

Pamela E. Mlynczak  
Science Applications International Corporation, Hampton, VA

G. Louis Smith  
National Institute of Aerospace, Hampton, VA

Paul W. Stackhouse, Jr.  
NASA Langley Research Center, Hampton, VA

Shashi K. Gupta  
Analytical Services and Materials, Inc., Hampton, VA

### ABSTRACT

The Surface Radiation Budget Data Set contains seven components describing radiation flux: shortwave up, down and net, longwave up, down and net, and total radiation net. A principal component analysis has been used to study the diurnal cycles of these components for an average July. The large thermal inertia of the ocean causes the diurnal cycle of its temperature to be quite small, so the globe was partitioned into land and ocean for this study. For each of the seven components, one principal component describes more than 97% of the variance of the diurnal cycle for land except for downward longwave flux, for which the first principal component describes 94% of the variance. The terms describing the remaining variance contain a mixture of physical effects and artifacts at a level of less than 1%. The downward and net shortwave fluxes are symmetric about noon, showing little effect of cloudiness with time of day. The upward, downward and net longwave fluxes have peaks in the afternoon, showing the lag of warming of the surface and atmosphere.

### 1. INTRODUCTION

The weather and climate system is driven by solar radiation and the subsequent emission of longwave radiation. There are two strong cycles of solar radiation: the annual cycle and the diurnal cycle. An examination of the response of the weather and climate system to radiative forcing at the annual and daily time scales provides insight into the processes which constitute the

weather and climate system. The annual cycle of radiation at the "top of the atmosphere" (TOA) has been studied by Smith et al. (1990) and Bess et al. (1992), and the diurnal cycle of outgoing longwave radiation at TOA has been reported by Smith and Rutan (2003). Understanding the response of a dynamical system to a cyclical forcing is fundamental to knowledge of the system's behavior. The nonlinear nature of the climate system requires that we use information about the diurnal cycle to help to characterize the system. One application of the results is to compare these results with the diurnal cycles that are computed by climate models. Another application is to provide information for solar power studies.

Most absorption of solar radiation occurs at the surface, where this radiation provides sensible heat and the energy for evapo-transpiration. The heating of the surface and atmosphere results in annual and diurnal cycles of the longwave radiation at the surface. The present paper examines the diurnal cycles of radiation fluxes at the surface using the Surface Radiation Budget Data Set (Gupta et al., 1999; 2004), which was developed by the Langley Research Center of NASA as part of the Global Energy and Water Experiment (GEWEX). This data set was used by Wilber et al. (2002; 2005) to investigate the annual cycles of radiation components at the surface. The diurnal cycles of each region are computed, and a principal component analysis is used to examine them. This method has the advantage of providing a very compact description of the diurnal cycles such that one may comprehend their temporal and geographic variations. The data set and the method of analysis are first described, after which the results are presented and discussed.

### 2. DATA

The Surface Radiation Budget (SRB) Data Set was developed in response to the need for such

---

*Corresponding author address:*

Pamela E. Mlynczak, SAIC, 1 Enterprise Parkway,  
Suite 300, Hampton, VA 23666.

E-mail: p.e.mlynczak@larc.nasa.gov

information by the climate research community (Suttles and Ohring, 1986). The data set used in the present study is SRB Release 2.1 (Gupta et al., 2004), which has a number of improvements over the earlier data set and covers a longer period. These improvements include a finer resolution of 1 degree in latitude and longitude (at the Equator) and improved cloud parameters, especially near the Sun-glint. Cloud properties are derived from the International Satellite Cloud Climatology Project DX data (Rossow and Schiffer, 1991). For less than 50% cloud cover, the skin temperature from ISCCP is used for computing upward longwave flux LWU. Temperature and humidity profiles are taken from the Goddard Earth Observing System-1 (GEOS-1) reanalysis project at six-hourly intervals starting at midnight GMT. For cloud cover greater than 50%, the surface temperature is taken from GEOS-1 also. Where ice or snow cover exceeds 80%, the ISCCP skin temperature is used. The ocean temperature is taken from the Reynolds' analysis once per week, and the diurnal cycle of ocean temperature is assumed to be negligible. The computed radiation fluxes are interpolated to give values at three-hour intervals.

The SRB Data Set includes the fluxes at the surface of insolation (shortwave radiation down, SWD), the reflected solar radiation (shortwave up, SWU), the radiation emitted by the atmosphere (longwave down, LWD), and the radiation emitted by the surface (longwave up, LWU). In addition, the shortwave net (SWN) and longwave net (LWN), which are the differences of the up and down components, and the total net (TN), which is the difference between the SWN and LWN, are included. This data set gives global coverage with a quasi-equal angle grid approximating one degree resolution at the Equator for the period 1982 through 1993. The fields are archived for every three hours starting with midnight at Greenwich. The radiation budget terms (SWD, LWU, etc.) are computed for four times per day based on meteorology at GMT = 0600, 1200, 1800 and 2400 hours. These values are interpolated to get eight times per day, or every three hours in the SRB data set.

### 3. ANALYSIS METHOD

There are 44016 regions in the nested grid of the data set, each with three-hourly values for each parameter. These are regridded onto a 360° by 180° equal angle grid using replication. The first step in the analysis is to compute the mean for each term (SWD, LWU, etc.) for each of the eight

times of day for which data are given and for each grid box. For each of the eight times, the mean is computed for all days of July for all Julys in the period from 1982 through 1993.

The next step is to compute the values on the basis of local time for each grid box. For each integer hour of local time, the GMT is computed as local time minus four minutes (time) for every degree of latitude west of Greenwich. The value of each parameter is then given for local time by use of a cubic spline to interpolate between the GMT values. By using 24 local hour values based on eight, 16 dependent values are introduced. However, the results will show that the 24 values describe the diurnal cycles better than eight values can. The daily mean value is then computed and subtracted from the 24 values to form the diurnal cycle.

In order to examine the regions, principal component analysis is used. Because of the enormous thermal inertia of the ocean, the diurnal cycle over the ocean is much smaller than over land; thus land and ocean regions are treated separately. Regions with mixed land and ocean are excluded. A 24x24 covariance matrix is computed as

$$M = S D(t,x) D(t',x),$$

where  $D(t,x)$  denotes the diurnal cycle at time of day  $t$  for region  $x$  and the summation is over all of the land regions  $x$ . The eigenvalues  $\lambda_i$  and the eigenvectors, i.e. the principal components  $PC_i(t)$ , of this covariance matrix are computed. Finally the empirical orthogonal functions  $EOF_i(x)$  are computed by projecting the 24  $PC_i(t)$  onto the 24 hourly maps for each parameter. The temporal and geographical variations of the diurnal cycle of a parameter are then given by

$$D(t,x) = \sum PC_i(t) EOF_i(x).$$

### 4. RESULTS AND DISCUSSION

The ocean regions have a small diurnal cycle compared to land, due to its immense thermal mass; thus, the diurnal cycle of land will be studied, then that for ocean.

Land: There are seven radiation parameters considered. Table 1 lists for land the root-mean-square RMS of the diurnal cycle of each of these parameters and the first three eigenvalues of the covariance matrix. These eigenvalues have been normalized by dividing by the trace of the covariance matrix so that their sum is one. The

RMS of SWD is  $232 \text{ W}\cdot\text{m}^{-2}$ , which may be compared to the mean insolation at the top of the atmosphere of  $342 \text{ W}\cdot\text{m}^{-2}$ , i.e. the solar output divided by 4. The RMS for SWU is  $51.5 \text{ W}\cdot\text{m}^{-2}$ , corresponding to a mean albedo of 0.22 for land. Note that  $\text{SWU} + \text{SWN} = 238$ , which does not equal the RMS for SWD but is close. For longwave, LWN is an order of magnitude smaller than SWN and has a small phase lag, which implies a low effective thermal mass, indicating that most of the heat from surface net insolation is transferred to the atmosphere as sensible or latent heat.

Table 1: Root-mean-square of radiation parameters ( $\text{W}\cdot\text{m}^{-2}$ ) and eigenvalues (dimensionless) for land

| Parameter | RMS  | $\lambda_1$ | $\lambda_2$ | $\lambda_3$ |
|-----------|------|-------------|-------------|-------------|
| SWD       | 232  | 0.984       | 0.013       | 0.002       |
| SWU       | 51.5 | 0.977       | 0.011       | 0.008       |
| SWN       | 187  | 0.981       | 0.014       | 0.002       |
| LWD       | 21.5 | 0.926       | 0.036       | 0.017       |
| LWU       | 40.2 | 0.975       | 0.013       | 0.007       |
| LWN       | 22.5 | 0.945       | 0.023       | 0.018       |
| Total Net | 170  | 0.980       | 0.015       | 0.002       |

The matrix is  $24 \times 24$ , so that there are 24 eigenvalues. However, the 24 hourly values are created by interpolation from a set of eight values, so that 16 values are dependent on the original eight values. Thus the additional 16 eigenvalues are expected to be null, and one expects only eight non-zero eigenvalues. For each of the seven parameters the first eigenvalue is greater than 0.92, leaving very little power for the remaining terms, indicating that the first principal component describes the diurnal cycle very well.

Figure 1 shows the first four principle components for SWD as a function of local time. The symmetry of PC-1 for SWD about noon shows that globally any effects of meteorology on the SWD (i.e. cloudiness variations from morning to afternoon) are quite small. Simplistically, the shape is the cosine of the solar zenith angle. However, the time of sunrise varies with latitude, so that the curve does not have a break in slope at sunrise and sunset as it would at a single latitude, but has a continuous slope on both sides. The second principal component PC-2 for SWD is a two-wave, with maxima at the zero crossings of PC-1 and a minimum at noon. The effect of this term is to broaden or narrow the contribution of PC-1 with a change in latitude to produce longer days at high northern latitudes and shorter days at

high southern latitudes. The third principal component is skew-symmetric about noon and describes the effects of morning versus afternoon cloudiness. This term accounts for only 0.2% of the power in the SWD diurnal variation.

The geographical distribution that corresponds to PC-1 for SWD is EOF-1 and is shown by fig. 2. Insolation at the "top of the atmosphere" is a function of latitude only, so that the longitudinal variation is due to clouds. The greatest amount of sunlight is over the Sahara Desert and the deserts of the Middle East, where there are few clouds. In July, the monsoons over India reduce the SWD at the surface. Likewise, in July the deep convection zone of equatorial Africa has moved north of the Congo Basin and the Congo has high surface insolation, and the deep convection zone of equatorial South America has moved north, leaving the Amazon Basin with high surface insolation. For July, the insolation is small over the Antarctic. The EOF-2, corresponding to PC-2, which is a two-wave, is not shown but is a function primarily of latitude.

SWU is given by SWD times surface albedo, and SWN is given by SWD times  $(1 - \text{albedo})$ . The geographical distributions for SWU and SWN are different from that of SWD due to the albedo map. As a consequence, the shapes of the principal components differ, though very slightly, from those for SWD. Figure 3 shows the first four principal components of SWN. Because SWN is the radiation flux absorbed at the surface, it is the component of primary interest for climate studies. Figure 4 shows EOF-1 for SWN. The Sahara Desert has a large value for SWN, but is not nearly as large as the value for SWD because of the high albedo of this area. For Greenland, the SWN is quite small due to the very high albedo of the ice cover. The value for the Antarctic is small due to the small SWD and the high albedo.

The net shortwave flux heats the surface, raising its temperature to create a diurnal cycle of upward longwave flux and also heating the air above as well as providing latent heat for evapotranspiration. Figure 5 shows the principal components for LWU. The first principal component is similar to that for the SWN during the day but has a definite lag of the peak value by about  $1 \frac{1}{4}$  hours after noon and continues to decrease at a slow rate from sunset to sunrise. The geographic distribution of the LWU, EOF-1, is shown by fig. 6. The Sahara Desert and deserts of the Middle East have the largest diurnal cycles, followed by other deserts and steppe regions. Although PC-2 accounts somewhat for the variation of length of day with latitude, the

geographic variation of EOF-2 shows that PC-2 is heavily influenced by the interpolation to get hourly values to describe the diurnal cycle. One advantage of the principal component method is that the results help to separate artifacts, like those due to interpolation to get hourly values.

The principal components for LWD are shown by fig. 7. The PC-1 is smoother than that for LWU, and the peak is at 1400 hours, as the temperature of the atmosphere requires an additional time lag for its response to heating from the surface. There is a small amount of absorption of solar radiation within the air, which will be in phase with the SWD. The time response for this directly absorbed radiation is shorter than for that which is absorbed at the surface and transferred by mixing into the atmosphere. An examination of EOF-2 shows that PC-2 is an artifact due to the time-interpolation to form the hourly values. Figure 8 shows the EOF-1 for LWD. As with LWU, the largest values are over the Sahara Desert and the deserts of the Middle East, after which the steppes are prominent.

Figure 9 shows the first four principal components of LWN. The PC-1 accounts for 94% of the variance and has a peak at 1300 hours local time. Figure 10 shows the map of the first EOF of LWN. Negative net longwave radiation corresponds to cooling at the surface. Therefore, as expected, the largest negative values in EOF-1 are over the deserts of the Middle East, followed by the Sahara Desert, the deserts and steppe of the U. S., the deserts and steppe east of the Himalayas and Tibetan Plateau in the Northern Hemisphere, and the Kalahari and Australian Deserts in the Southern Hemisphere. For LWN, PC-1 and PC-2 describe the increase of length of day with increasing northern latitude. Their eigenvalues are close to each other: 0.023 and 0.018, respectively. Examination of EOF-2 shows some latitudinal structure, which can be interpreted as describing the length of day variation, but it also shows some longitudinal structure that may be artifacts of interpolation. EOF-3 is a latitudinal variation corresponding to the variation of length of day, with small longitudinal variations that also suggest artifacts due to interpolation.

**Ocean:** For ocean, there is no significant temperature diurnal cycle; consequently the diurnal cycle of LWU can be ignored. Because of the absorption of solar radiation by the atmosphere and variations of cloud cover, there is a significant but small diurnal cycle of LWD over the oceans. The diurnal cycle of LWN is the same as that for LWD.

Table 2 lists the RMS values for the shortwave components, LWD and the total net radiative flux over ocean. The RMS for SWD over ocean is smaller than that for land. The SWU is smaller because of the low albedo of the ocean (0.06). The first PC of SWD, SWN and total net describe nearly 99% of the power of these parameters. LWD is small, and the first PC only accounts for 72% of its power.

Table 2: Root-mean-square of radiation parameters ( $W\cdot m^{-2}$ ) and eigenvalues for ocean

| Parameter | RMS  | $\lambda_1$ | $\lambda_2$ | $\lambda_3$ |
|-----------|------|-------------|-------------|-------------|
| SWD       | 215  | 0.988       | 0.008       | 0.001       |
| SWU       | 13.3 | 0.932       | 0.026       | 0.020       |
| SWN       | 204  | 0.988       | 0.008       | 0.001       |
| LWD       | 3.9  | 0.716       | 0.138       | 0.055       |
| Total Net | 202  | 0.988       | 0.008       | 0.001       |

Figure 11 shows the first four principal components of SWD, which are very similar to those for land. Again, the first term resembles the cosine of the solar zenith angle with rounded transitions at sunrise and sunset, and the second term provides the variation of length day with latitude. Figure 12 is EOF-1 for SWD. It is quite latitudinal, but the subsidence areas of the oceans appear as having strong SWD at the surface where there is little cloud cover. In July, the subsidence areas are strongest in the Northern Hemisphere. The SWU and SWN differ in magnitude from SWD by the albedo for SWU and by  $(1 - \text{albedo})$  for SWN but have the same pattern in time and geographically.

Figure 13 shows the first four principal components for LWD over ocean. The total range is only 1% of that of SWD, and at this low level the effects of errors must be considered. Figure 14 shows the map of the first EOF of LWD. The oval at the date line is a clear artifact and is due to the lack of coverage by geostationary spacecraft. It is too far west for GOES observations and too far east for viewing by the Japanese Geosynchronous Meteorological Satellite (GMS). Likewise, there is a feature shaped like an hourglass in the neighborhood of  $75^\circ E$ , where there is a gap between GMS and the European MeteoSat. These artifacts are similar to features with which the producers and users of the ISCCP and Surface Radiation Budget data sets are familiar. Nevertheless, in regions for which there is good coverage by the geostationary spacecraft, the results appear to have validity. The high EOF-1 values at the eastern sides of the North Pacific Ocean and a bit of the North Atlantic Ocean next

to Africa correspond to areas that have morning cloudiness. At 30° north and south there are negative bands, which would indicate clearing of clouds during the day, thus reducing LWD.

## 5. CONCLUSIONS

The diurnal cycles of surface radiation fluxes have been investigated by use of principal component analysis. These fluxes are shortwave up, down and net, longwave up, down and net and total net fluxes. The diurnal cycle of longwave radiation is much greater over land than over ocean due to the great thermal mass of the ocean, thus land and ocean were separated for the study. The month of July was selected for this study, as there is more land in the Northern Hemisphere than in the Southern, and the shortwave diurnal cycle is maximum in July. The first principal component in each case describes more than 97% of the variance except for longwave down and net fluxes. The asymmetries about noon are very small for shortwave fluxes, showing that globally the effects on shortwave fluxes due to cloudiness variations from morning to afternoon are small. Geographically the longwave diurnal cycles are largest over the Sahara and other deserts, decreasing through steppes and then to temperate regions and becoming quite small over snow covered regions such as Greenland. The second principal component describes variation of length of day with latitude.

## ACKNOWLEDGEMENTS

The authors gratefully acknowledge support by the Surface Radiation Budget Program from the NASA Office of Science through the Langley Research Center to Science Applications International Corporation and to the National Institute of Aerospace. They also acknowledge the Atmospheric Sciences Data Center of Langley Research Center for access to the data set.

## REFERENCES

- Bess, T. D., G. L. Smith, T. P. Charlock and F. G. Rose, 1992: Annual and interannual variations of Earth-emitted radiation based on a 10-year data set. *J. Geophys. Res., Atmos.*, **97**, 12825-12835.
- Gupta, S. K., N. A. Ritchey, A. C. Wilber, C. H. Whitlock, G. G. Gibson, and P. W. Stackhouse. 1999: A climatology of surface radiation budget derived from satellite data., *J. Climate*, **12**, 2691-2710.
- Gupta, S. K., P. W. Stackhouse, S. J. Cox, J. C. Mikovitz and M. Chiacchio, 2004: The NASA/GEWEX Surface Radiation Budget Data Set, Preprint, *13th Conf. on Satellite Meteorology and Oceanography*, Norfolk, VA, Amer. Meteor. Soc., CD-ROM, P6.6.
- Rossow, W. B. and R. A. Schiffer, 1991: ISCCP cloud data products, *Bull. Amer. Meteor. Soc.*, **72**, 2-20.
- Smith, G. L. and D. Rutan, 2003: The diurnal cycle of outgoing longwave radiation from Earth Radiation Budget Experiment measurements, *J. Atmos. Sci.*, **60**, 1529-1542.
- Smith, G. L., D. Rutan, T. P. Charlock and T. D. Bess, 1990: Annual and interannual variations of absorbed solar radiation based on a 10-year data set., *J. Geophys. Res., Atmos.*, **95**, 16639-16652.
- Suttles, J. T. and G. Ohring, 1986: Surface radiation budget for climate applications, NASA Reference Publication 1169, NASA, Washington D.C., 132pp.
- Wilber, A. C., G. L. Smith and P. W. Stackhouse, 2002: Seasonal cycles of surface radiation budget and climate classes, Preprint, *13<sup>th</sup> Symposium on Global Change and Climate Variations*, Orlando, FL, Amer. Meteor. Soc., 2.10.
- Wilber, A. C., G. L. Smith, S. Gupta and P. W. Stackhouse, 2005: Annual cycle of surface shortwave radiation, accepted by *J. Climate*.

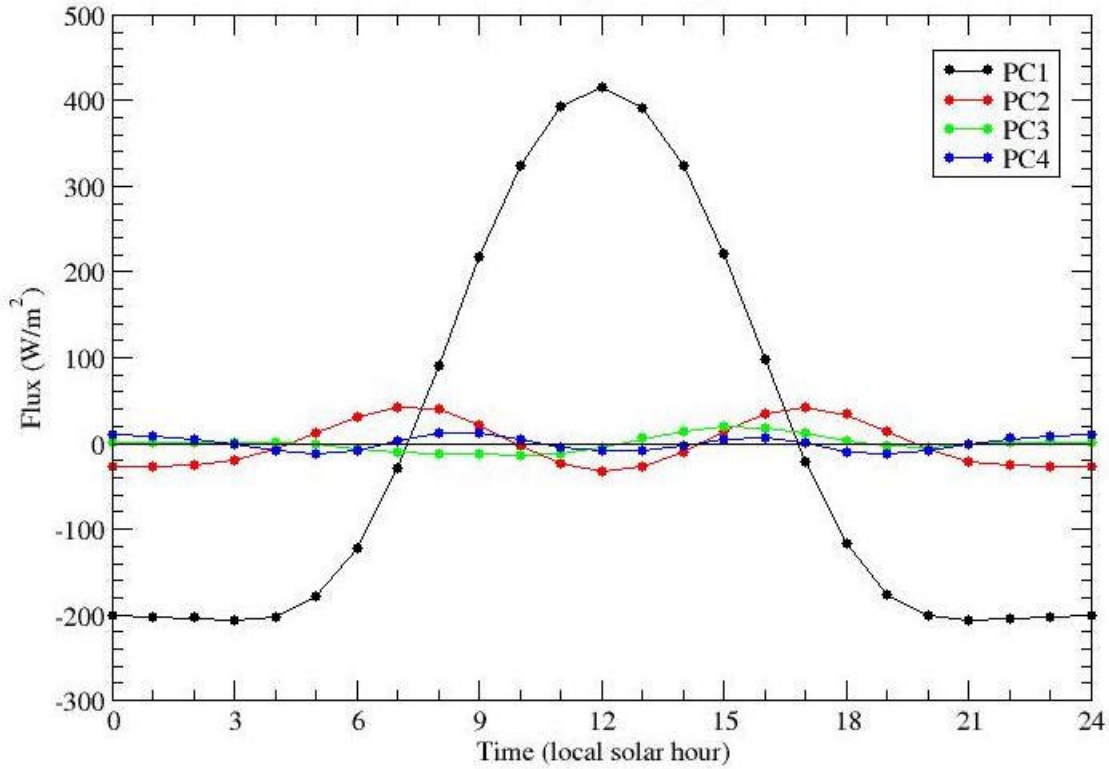


Figure 1: First four principal components of downward shortwave flux SWD in  $W\cdot m^{-2}$  over land for July.

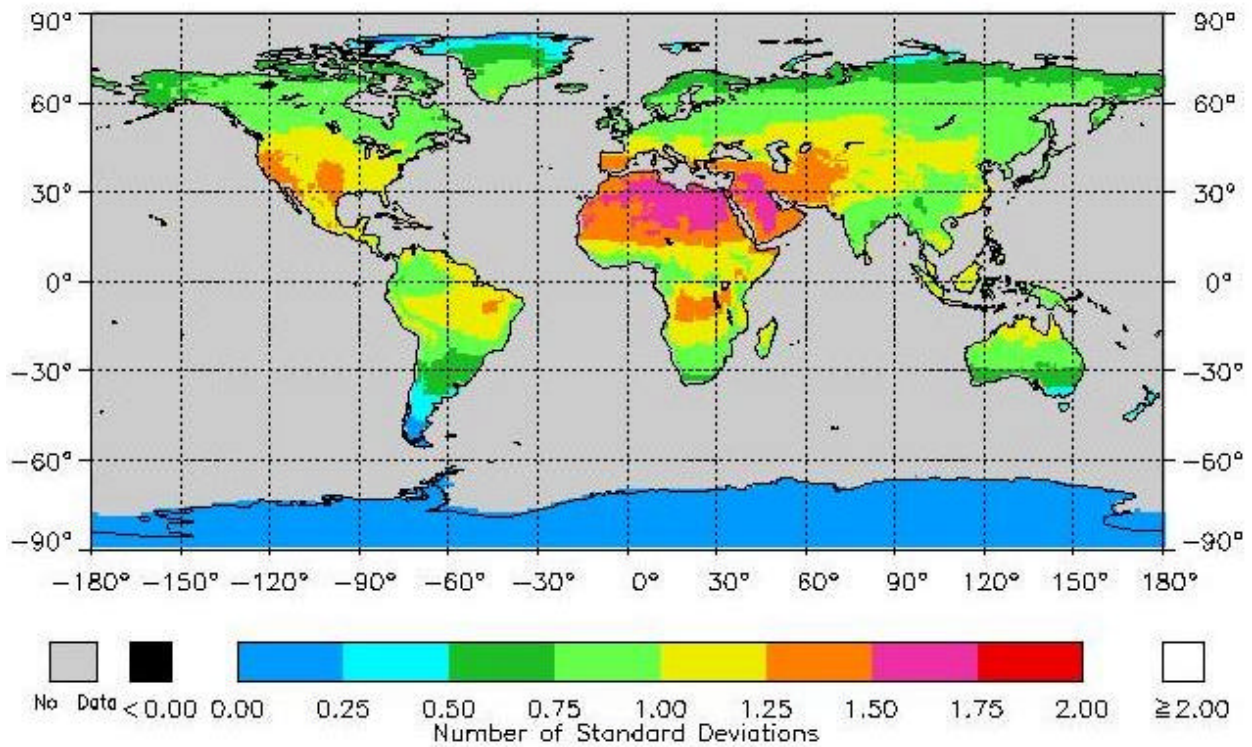


Figure 2: First EOF of downward shortwave flux SWD in  $W\cdot m^{-2}$  over land for July.

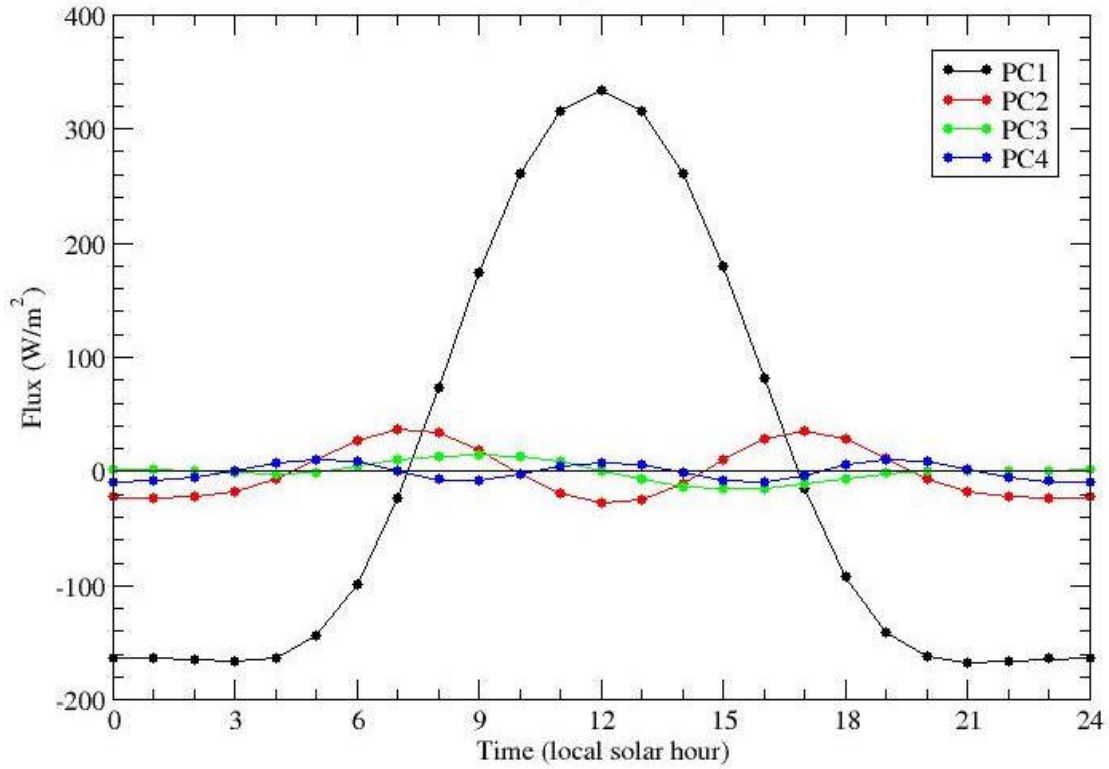


Figure 3: First four principal components of net shortwave flux SWN in  $W\cdot m^{-2}$  over land for July.

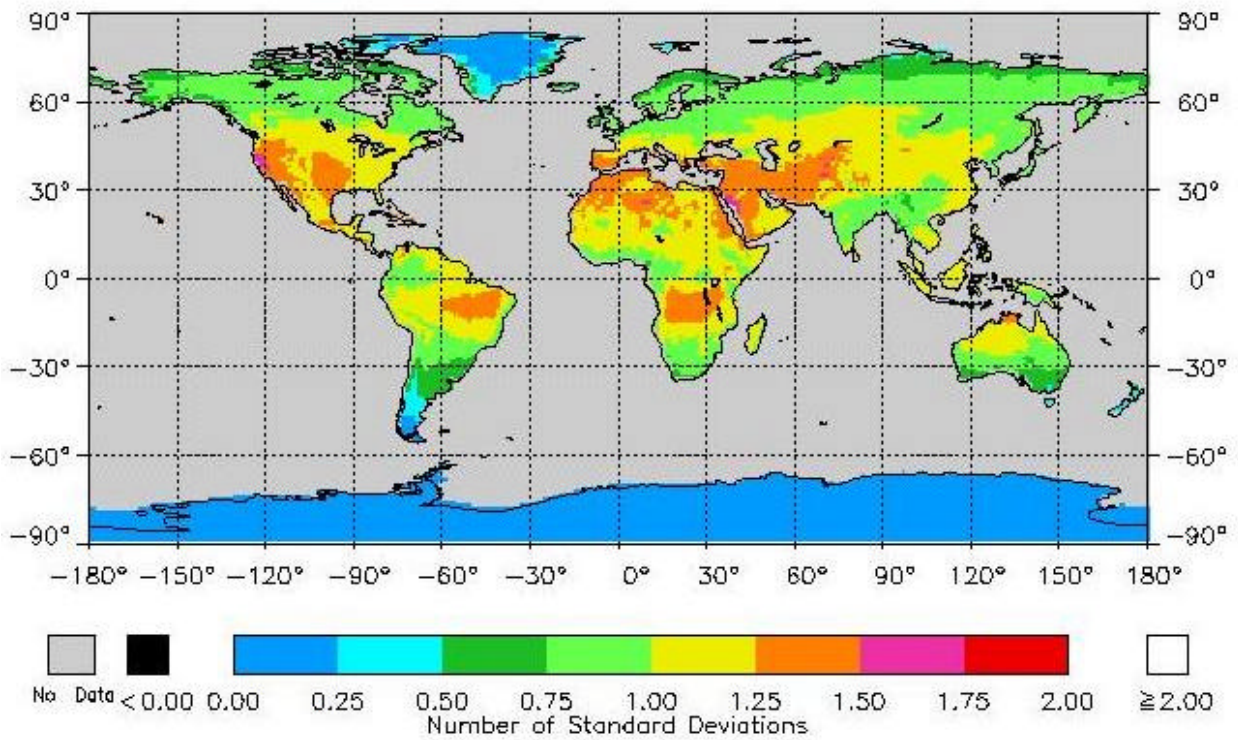


Figure 4: First EOF of net shortwave flux SWN in  $W\cdot m^{-2}$  over land for July.

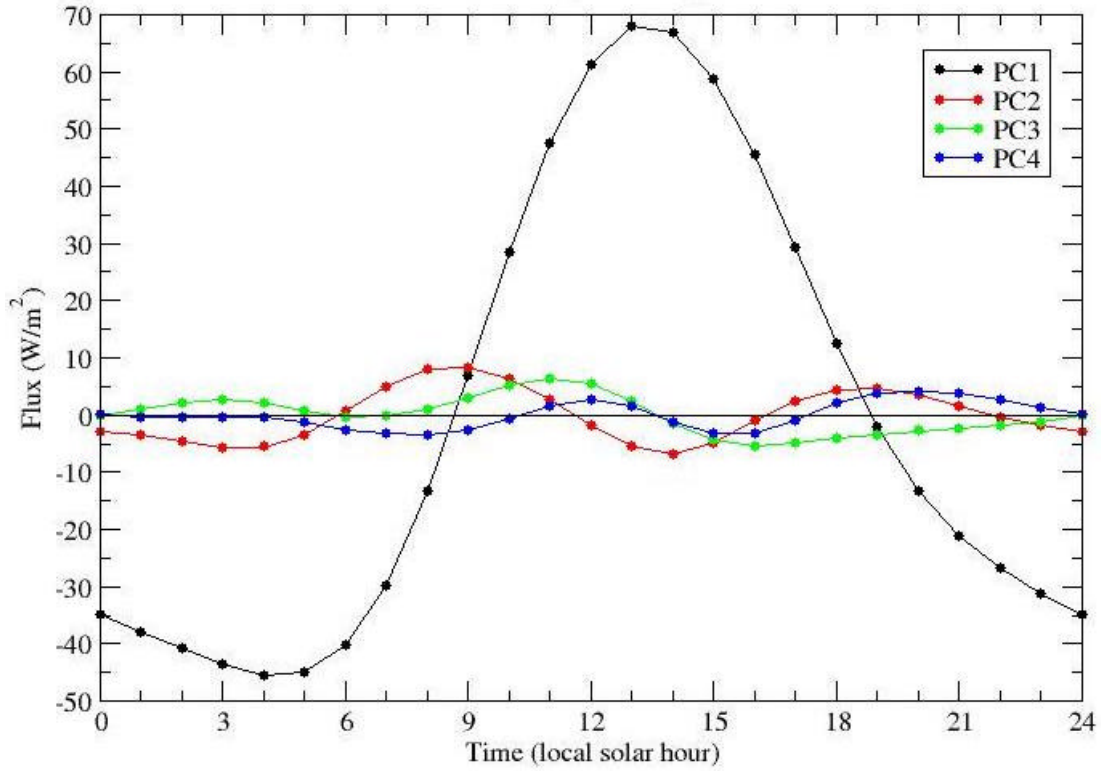


Figure 5: First four principal components of upward longwave flux LWU in  $W\cdot m^{-2}$  over land for July.

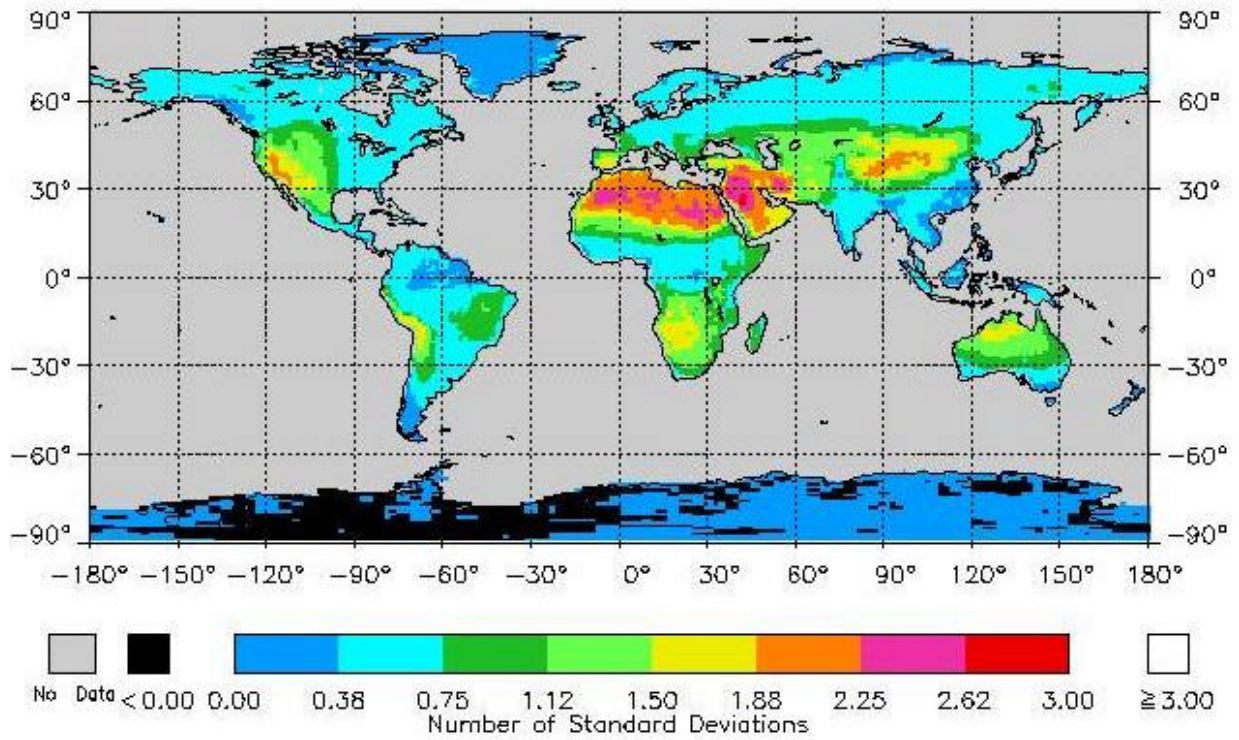


Figure 6: First EOF of upward longwave flux LWU in  $W\cdot m^{-2}$  over land for July.

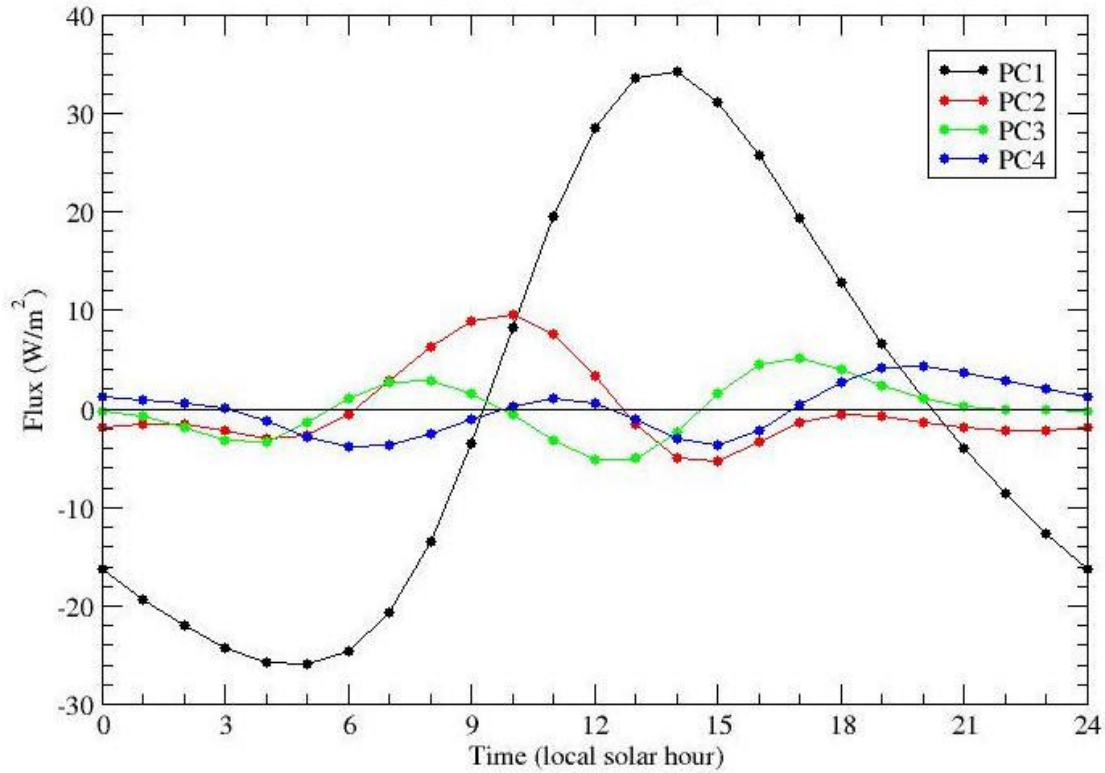


Figure 7: First four principal components of downward longwave flux LWD in  $W\cdot m^{-2}$  over land for July.

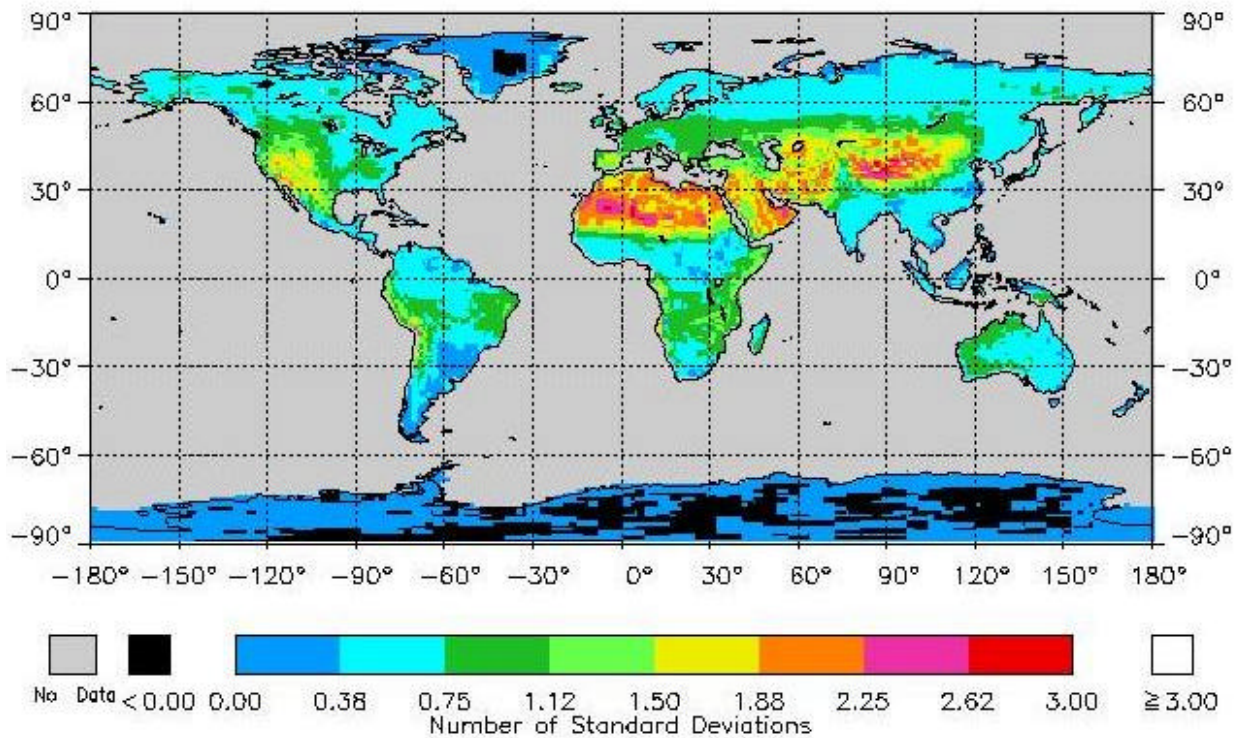


Figure 8: First EOF of downward longwave flux LWD in  $W\cdot m^{-2}$  over land for July.

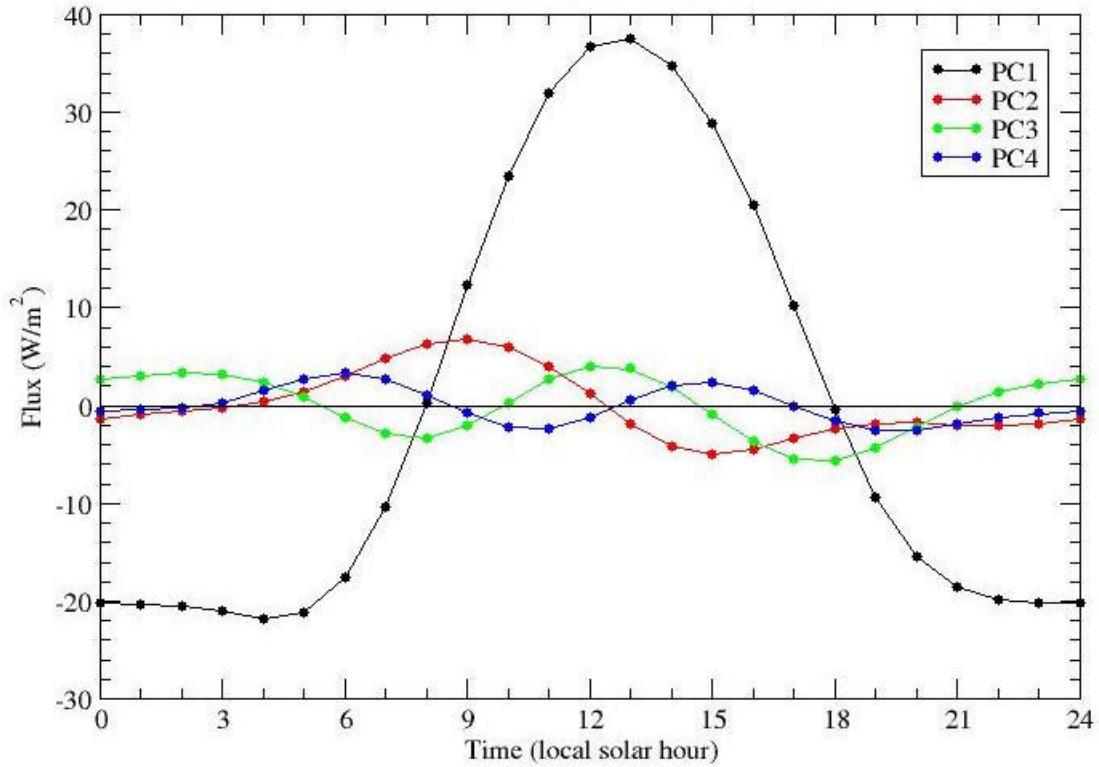


Figure 9: First four principal components of net longwave flux LWN in  $W\cdot m^{-2}$  over land for July.

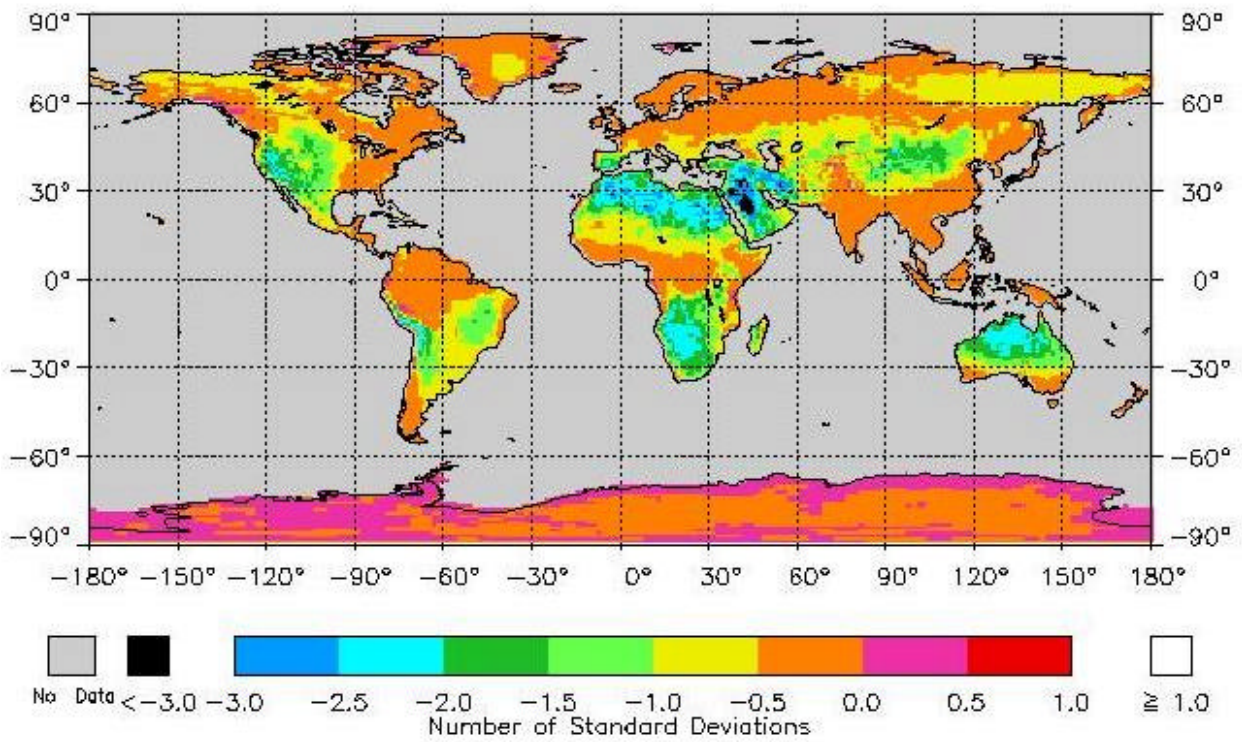


Figure 10: First EOF of net longwave flux LWN in  $W\cdot m^{-2}$  over land for July.

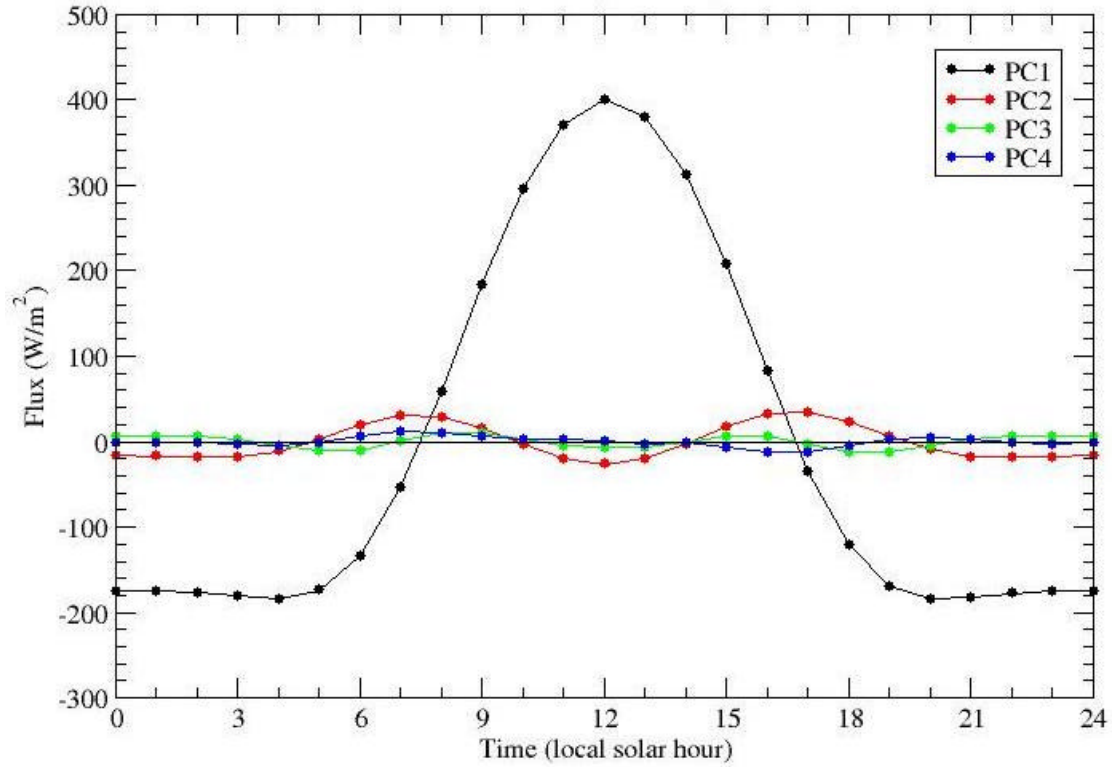


Figure 11: First four principal components of downward shortwave flux SWD in  $W\cdot m^{-2}$  over ocean for July.

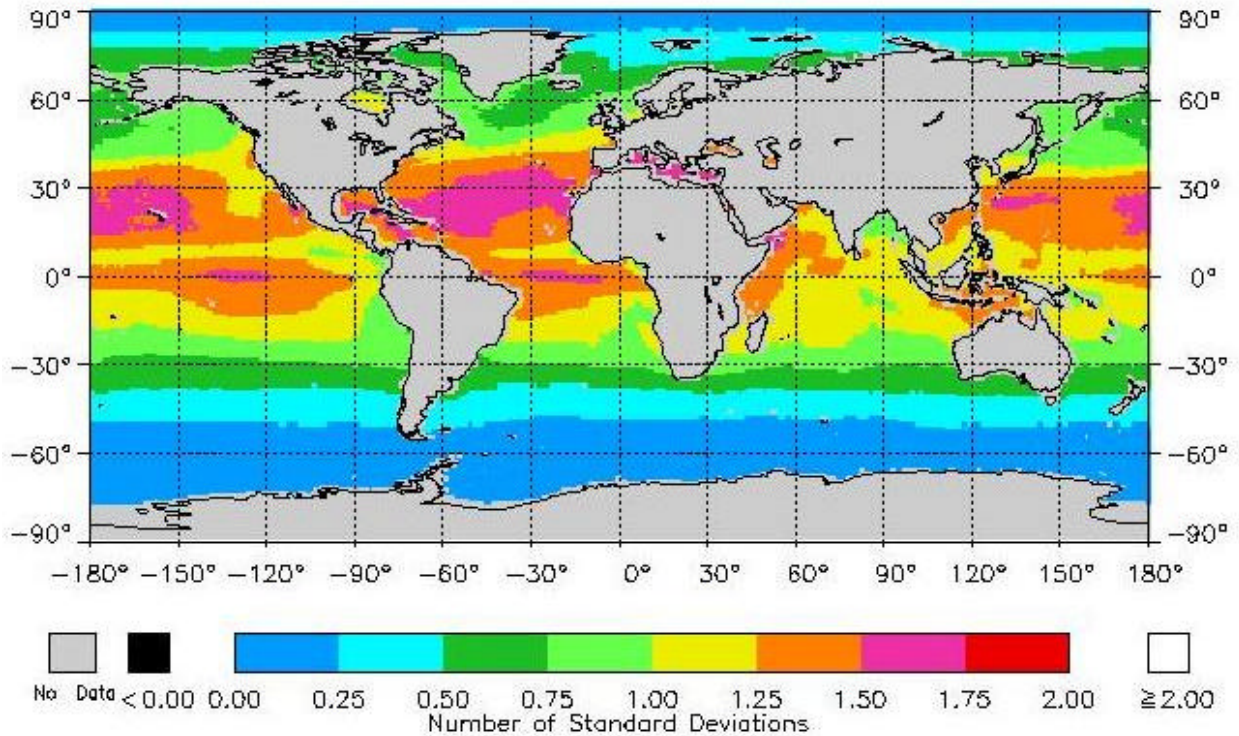


Figure 12: First EOF of downward shortwave flux SWD in  $W\cdot m^{-2}$  over ocean for July.

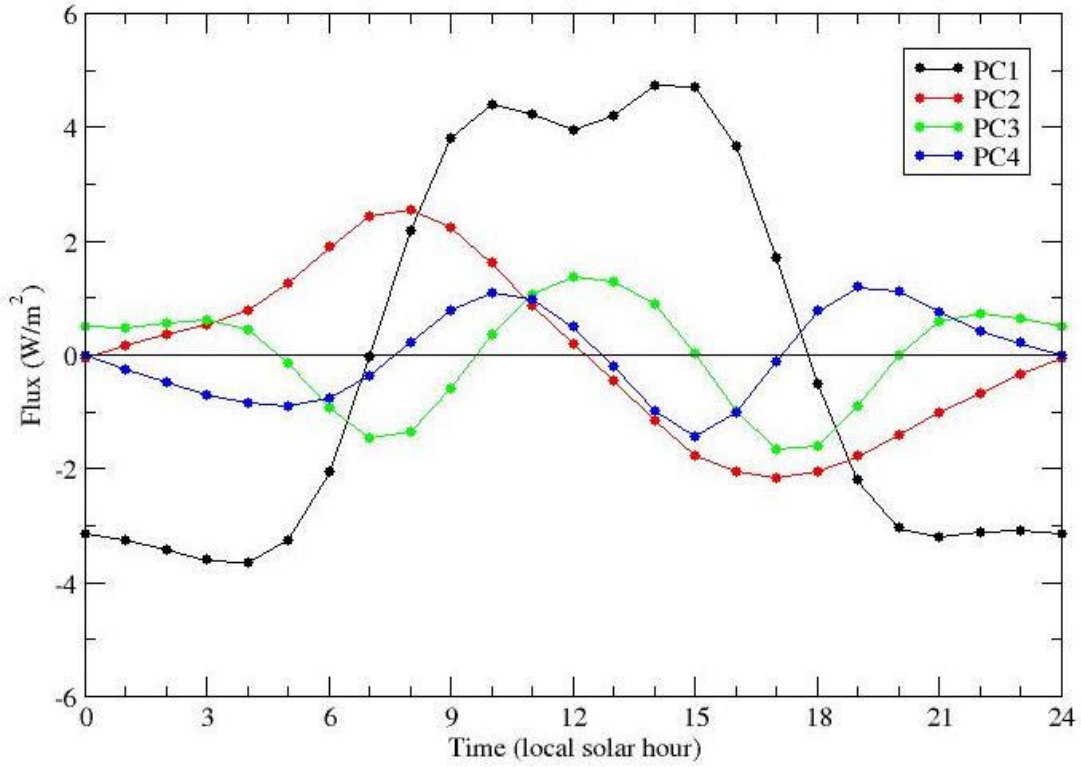


Figure 13: First four principal components of downward longwave flux LWD in  $\text{W}\cdot\text{m}^{-2}$  over ocean for July.

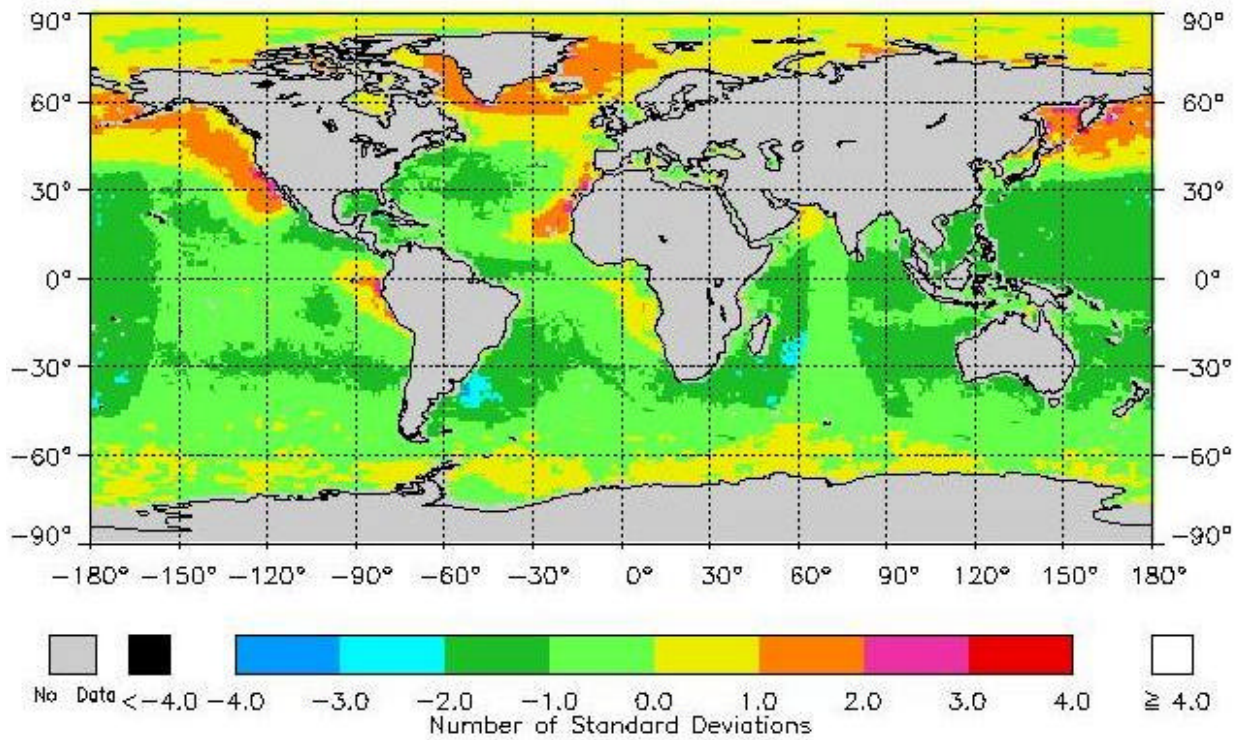


Figure 14: First EOF of downward longwave flux LWD in  $\text{W}\cdot\text{m}^{-2}$  over ocean for July.